

# Supplemental Information: Magnetic Phase Transitions and Spin Density Distribution in the Molecular Multiferroic GaV<sub>4</sub>S<sub>8</sub> System

Rebecca L. Dally,<sup>1</sup> William D. Ratcliff II,<sup>1,2</sup> Lunyong Zhang,<sup>3,4</sup> Heung-Sik Kim,<sup>5,6</sup> Markus Bleuel,<sup>1,2</sup>

J. W. Kim,<sup>6,7</sup> Kristijan Haule,<sup>6</sup> David Vanderbilt,<sup>6</sup> Sang-Wook Cheong,<sup>3,6,7</sup> and Jeffrey W. Lynn<sup>1</sup>

<sup>1</sup>*NIST Center for Neutron Research, National Institute of Standards and Technology, Gaithersburg, MD 20899-6102*

<sup>2</sup>*Department of Materials Science and Engineering, University of Maryland, College Park, MD 20742*

<sup>3</sup>*Laboratory for Pohang Emergent Materials, Pohang Accelerator Laboratory and Max Plank POSTECH Center for Complex Phase Materials, Pohang University of Science and Technology, Pohang 790-784, Korea*

<sup>4</sup>*School of Materials Science and Engineering, Harbin Institute of Technology, Harbin, 150001, China*

<sup>5</sup>*Department of Physics, Kangwon National University, Chuncheon 24341, Republic of Korea*

<sup>6</sup>*Department of Physics and Astronomy, Rutgers University, Piscataway, NJ 08854*

<sup>7</sup>*Rutgers Center for Emergent Materials, Rutgers University, Piscataway, NJ 08854*

(Dated: June 15, 2020)

## BULK SUSCEPTIBILITY

Fig. S1 shows the 91.1 mg single crystal sample used throughout this study, along with the zero-field cooled (ZFC) bulk susceptibility measurements used to initially characterize the magnetic transition temperatures. The data show well-defined magnetic transitions at  $T = 13.5$  K and  $T = 6.7$  K, corresponding to cycloidal long-range order and ferromagnetic order, respectively, and consistent with previous research. [1] The transitions are even more pronounced in the susceptibility derivative,  $d\chi/dT$ , shown on the right axis of Fig. S1.

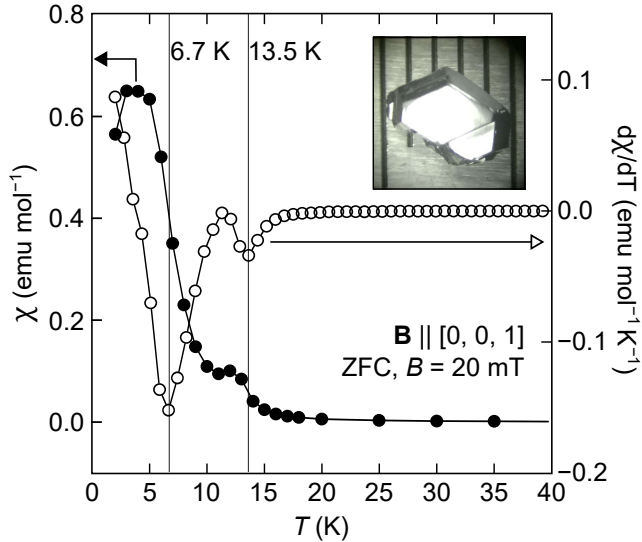


FIG. S1. Zero-field cooled (ZFC) bulk susceptibility measurements on the crystal used throughout the study, which is shown in the inset and was massed at 91.1 mg. The data show well-defined magnetic transitions at  $T = 13.5$  K and  $T = 6.7$  K, corresponding to cycloidal long-range order and ferromagnetic order, respectively. The transitions are even more pronounced in the susceptibility derivative,  $d\chi/dT$ , shown on the right axis. Note:  $1 \text{ emu} = 10^{-3} \text{ A m}^2$ .

## FORM FACTOR CALCULATIONS

The single unpaired electron within a  $V_4$  molecular cluster is responsible for the magnetic and ferroelectric properties in GaV<sub>4</sub>S<sub>8</sub>. Knowing the charge distribution for this unpaired electron within the  $V_4$  cluster will guide calculations and understanding of similar systems, and this is the basis for performing the form factor measurements presented in this manuscript. The unpaired electron has a spin, and because neutrons have a magnetic moment, they will interact with unpaired electrons via the dipole-dipole interaction. This contrasts with x-ray scattering (off resonance), where x-rays will interact with all of the electrons in a system, not just those unpaired.

The structure factor for magnetic Bragg scattering,  $F_M(\mathbf{Q})$ , includes the term,  $\mu f(\mathbf{Q})$ , which is the magnetic moment multiplied by the magnetic form factor, and  $\mathbf{Q}$  is the scattering vector. The magnetic form factor is the Fourier transform of the real-space magnetization density and is responsible for the decrease in magnetic intensity with increasing  $Q$ . The magnetic structure factor can be written as,

$$F_M(\mathbf{Q}) \propto \sum_i \mu_i f_i(\mathbf{Q}) \mathbf{P} \cdot \left[ \hat{\mathbf{Q}} \left( \hat{\mathbf{Q}} \cdot \hat{\boldsymbol{\mu}}_i \right) - \hat{\boldsymbol{\mu}}_i \right] \exp(i\mathbf{Q} \cdot \mathbf{R}_i) \quad (1)$$

where  $\mathbf{P}$  is the neutron polarization and  $\mathbf{R}_i$  is the real-space position of atom  $i$  in the unit cell, and the sum is over all atoms in the unit cell. Because  $\mu f(\mathbf{Q})$  is the quantity we are trying to evaluate, it can be taken as a variable in the following calculations. Assuming a magnetized ferromagnet, or a field-polarized paramagnet, the requirements for the measurement and ensuing calculation are to determine the flipping ratio,  $R(\mathbf{Q}) = I^{++}/I^{--}$ , obtained from polarized neutron diffraction measurements at a series of Bragg peaks with  $\mathbf{P} \perp \mathbf{Q}$  and the moments parallel to  $\mathbf{P}$  (where  $I^{++}$  and  $I^{--}$  are the two non-spin flip cross-section intensities).

The flipping ratio also depends on the nuclear structure factor,  $F_N(\mathbf{Q})$ , for the Bragg peaks measured, which can be calculated from the known crystal structure. The form factor can then be determined from the measured flipping ratio in terms of the nuclear and magnetic structure factors,

$$R(\mathbf{Q}) = \frac{I^{++}}{I^{--}} = \frac{|F_N + F_M|^2}{|F_N - F_M|^2}. \quad (2)$$

When evaluating Eq. 2, it is important to remember that the nuclear and magnetic structure factors are complex (i.e.  $F_N(\mathbf{Q}) = F_N^{Re}(\mathbf{Q}) + iF_N^{Im}(\mathbf{Q})$ ). For a more complete description of form factor measurements see, for example, Ch. 2 in Ref. [2].

In Table SI, we have calculated the theoretical values for  $R(\mathbf{Q})$  assuming the cubic unit cell with the single electron evenly distributed between the  $V_4$  cluster with  $\mu = 0.25 \mu_B/V$  and  $f(\mathbf{Q}) = 1$ . With no magnetic contribution the flipping ratio is of course unity, and here we note that the flipping ratios for the  $(1, 1, 1)$ -type peaks are opposite to most of the other peaks, which simply comes from the phase factors of the magnetic structure. We had hoped that this result would be qualitatively different if the moment resided solely on the apical V, but that turned out not to be the case for the peaks with a measurable magnetic signal.

Going further, and to understand our  $T = 3$  K high instrumental resolution data, we calculated the flipping ratios at various reflections while taking into account the four rhombohedral crystallographic domains. A schematic showing the domains with respect to each other, and to the neutron scattering plane is shown in Fig. S2, where the arrows represent the four equivalent directions that the cubic unit cell can be stretched below the Jahn-Teller distortion temperature. The domains are

TABLE SI. Calculated flipping ratio values for various Bragg peaks assuming a single electron is evenly distributed between the  $V_4$  cluster. The values calculated include just the structures factors (i.e.  $f(\mathbf{Q}) = 1$  for all  $\mathbf{Q}$ ).

$H, K, L$ (r.l.u.)	$ F_N + F_M ^2$	$ F_N - F_M ^2$	$R(\mathbf{Q})$
1, 1, 1	6.11	12.24	0.50
0, 0, 2	4.84	2.82	1.71
2, 2, 0	9.26	8.51	1.09
1, 1, 3	9.15	6.72	1.36
2, 2, 2	81.28	118.63	0.69
0, 0, 4	41.03	20.25	2.03
3, 3, 1	10.36	13.97	0.74
2, 2, 4	11.12	9.19	1.21
3, 3, 3	4.54	7.55	0.60
4, 4, 0	143.85	106.29	1.35

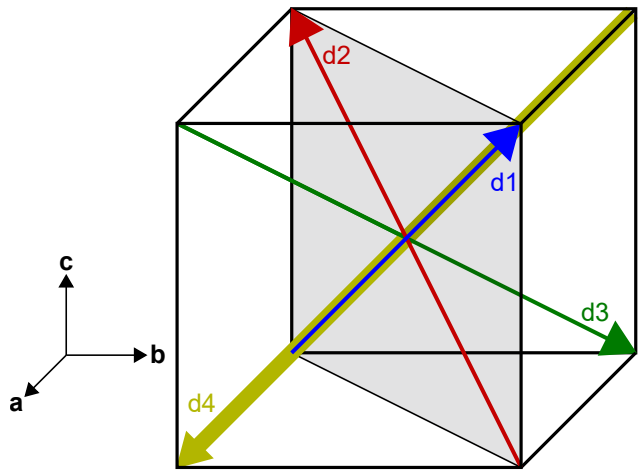


FIG. S2. Schematic of the orientations of each rhombohedral domain (d1–d4) with respect to the cubic structure. The cube outlined in black, and the crystallographic axes, represent the undistorted cubic crystal. The arrows show the different directions along which the cubic structure gets distorted. The direction of the arrows is also the direction that the spins align along for the different domains in the ferromagnetic phase. The gray plane shown is the scattering plane,  $(H, H, L)$ , which was used for the neutron experiments.

labeled d1–d4, and the gray plane shown is the  $(H, H, L)$  scattering plane in the cubic notation. The result of the domains in reciprocal space is that some cubic peaks split along  $Q$  due to different reflections from different domains cutting into the scattering plane.

The flipping ratio calculations for various Bragg reflections are presented in Table SII, where the first column is a cubic  $(H, K, L)$  reflection and the second column contains the corresponding rhombohedral  $(H, K, L)$  reflections which contribute intensity about the cubic point. The rows are split according to  $Q$  value. The third column contains the flipping ratio values assuming all moments are field polarized along a vertically applied magnetic field with the unpaired electron within a  $V_4$  cluster evenly distributed. This is the same assumption as the calculations presented in Table SI. One can see the values are almost exactly the same as those assuming a cubic notation, further validating our use of the cubic unit cell for calculations presented in the main text. The fourth column presents calculations assuming the electron is distributed inhomogeneously between the basal and apical V atoms according to the DFT results, which predicted  $0.221 \mu_B/\text{basal V}$  and  $0.419 \mu_B/\text{apical V}$ . The calculations in Table SII used this distribution but scaled the total moment to be  $1 \mu_B$  in order to compare with the other models. The last column presents calculations assuming the electron is localized to the apical V, with a value of  $1 \mu_B$ . Neither the equal distribution or apical assumption can explain the flipping ratio values measured with high resolution, like those in Fig. 5(c) and (d) of

TABLE SII. Calculated flipping ratio values,  $R(Q)$ , for various Bragg peaks for three models: (1) assuming a single electron is evenly distributed between the  $V_4$  cluster ( $0.25 \mu_B/V$ ), (2) the inhomogeneous distribution of the electron from DFT calculations, where the values have been scaled so that the total moment adds up to  $1 \mu_B$  ( $0.204 \mu_B/\text{basal V}$ ;  $0.387 \mu_B/\text{apical V}$ ), and (3) the electron is located only on the apical V ( $1 \mu_B/\text{apical V}$ ). This table differs from Table SI, in that the four crystallographic domains were considered. The first column lists the pseudo-cubic ( $H, K, L$ ), and the second column lists the rhombohedral domains which contribute intensity around that point. The domains are grouped by equivalent  $Q$ 's. For example, the cubic  $(1, 1, 1)$  splits into two peaks. The lower  $Q$  peak is only due to the  $(1, 1, 1)$  peak from d1, but the higher  $Q$  peak is a superposition of d2, d3, and d4 Bragg peaks. The values calculated include just the structures factors (i.e.  $f(\mathbf{Q}) = 1$  for all  $\mathbf{Q}$ ).

'cubic' $H, K, L$	rhombohedral domain and corresponding $H, K, L$	$R(Q)$ ( $0.25 \mu_B/V$ )	$R(Q)$ ( $0.204 \mu_B/\text{basal V}$ ; $0.387 \mu_B/\text{apical V}$ )	$R(Q)$ ( $1 \mu_B/\text{apical V}$ )
1, 1, 1	d1 (1, 1, 1)	0.51	0.65	1.80
	d2 (0, 0, -1), d3 (0, -1, 0), d4 (-1, 0, 0)	0.50	0.47	0.35
0, 0, 2	d1 (1, 1, 0), d2 (1, 1, 0), d3 (-1, -1, 0), d4 (-1, -1, 0)	1.74	1.69	1.39
2, 2, 0	d1 (1, 1, 2), d2 (-1, -1, -2)	1.08	0.84	0.28
	d3 (1, -1, 0), d4 (-1, 1, 0)	1.10	1.41	4.58
1, 1, 3	d1 (2, 2, 1)	1.30	1.60	4.16
	d3 (-1, -2, 0), d4 (-2, -1, 0)	1.40	1.45	1.63
	d2 (1, 1, -1)	1.36	1.07	0.37
2, 2, 2	d1 (2, 2, 2)	0.67	0.67	0.66
	d2 (0, 0, -2), d3 (0, -2, 0), d4 (-2, 0, 0)	0.69	0.69	0.69
0, 0, 4	d1 (2, 2, 0), d2 (2, 2, 0), d3 (-2, -2, 0), d4 (-2, -2, 0)	2.03	2.03	2.03
3, 3, 1	d1 (2, 2, 3)	0.72	0.72	0.73
	d2 (-1, -1, -3)	0.75	1.00	3.90
	d3 (1, -2, 0), d4 (-2, 1, 0)	0.75	0.65	0.32
2, 2, 4	d1 (3, 3, 2)	1.29	1.53	3.48
	d3 (-1, -3, 0), d4 (-3, -1, 0)	1.21	1.00	0.44
	d2 (1, 1, -2)	1.20	1.46	3.54
3, 3, 3	d1 (3, 3, 3)	0.69	0.55	0.18
	d2 (0, 0, -3), d3 (0, -3, 0), d4 (-3, 0, 0)	0.65	0.71	1.06
4, 4, 0	d1 (2, 2, 4), d2 (-2, -2, -4)	1.37	1.35	1.28
	d3 (2, -2, 0), d4 (-2, 2, 0)	1.34	1.37	1.47

the main text. In those figures, the lower- $Q$  peak is only due to intensity coming from d1, and has a flipping ratio of  $\approx 1$ . This would be the case if the moments were not polarized along the applied field direction, but still along—or mostly along—the local  $[1, 1, 1]$ -like directions due to the uniaxial anisotropy. Evaluating the rest of the data with this assumption proved difficult with the high-resolution data, however, because of crystallite formation below the Jahn-Teller distortion as we discuss shortly.

The main text presented the results of only the 4 V model (with equal electron distribution) and apical only model. The differences in the flipping ratios between the DFT inhomogeneous electron distribution and the 4 V model are much smaller than between the 4 V model and apical only model. This is especially true as the moment size is reduced from saturation, as is the case at 20 K with a 2 T field. Fig. 3(a) of the main text shows the moment per V to be  $\approx 0.1 \mu_B$  at 20 K and 2 T,

and to illustrate the differences between the models with this total moment value, we present the corresponding flipping ratio calculations in Table SIII.

## CRYSTALLITE FORMATION

Four crystallographic domains form below the Jahn-Teller distortion, but we found that more than four crystallites are actually forming. The orientation of each crystallite with respect to one another leads to multiple Bragg peaks along the mosaic direction in reciprocal space. Fig. S3(a) shows an  $(H, H, L)$  map about the  $(0, 0, 4)$  point in cubic notation at  $T = 20$  K. It is expected that contributions to the Bragg scattering from the four different domains should all coincide at a single point in reciprocal space here, however multiple peaks are seen spanning the mosaic direction, meaning they all

TABLE III. Calculated flipping ratio values,  $R(Q)$ , for various Bragg peaks for three models, where the total moment used ( $0.4 \mu_B$ ) matches that extracted from the 20 K data at 2 T from Fig. 3(a) of the main text. The three models are: (1) assuming the moment is evenly distributed between the  $V_4$  cluster ( $0.1 \mu_B/V$ ), (2) the inhomogeneous distribution of the moment from DFT calculations, where the values have been scaled so that the total moment adds up to  $0.4 \mu_B$  ( $0.082 \mu_B/\text{basal V}$ ;  $0.155 \mu_B/\text{apical V}$ ), and (3) the moment is located only on the apical V ( $0.4 \mu_B/\text{apical V}$ ). This table differs from Table SI, in that the four crystallographic domains were considered. The first column lists the pseudo-cubic ( $H, K, L$ ), and the second column lists the rhombohedral domains which contribute intensity around that point. The domains are grouped by equivalent  $Q$ 's. For example, the cubic  $(1, 1, 1)$  splits into two peaks. The lower  $Q$  peak is only due to the  $(1, 1, 1)$  peak from d1, but the higher  $Q$  peak is a superposition of d2, d3, and d4 Bragg peaks. The values calculated include just the structures factors (i.e.  $f(\mathbf{Q}) = 1$  for all  $\mathbf{Q}$ ).

'cubic' $H, K, L$	rhombohedral domain and corresponding $H, K, L$	$R(Q)$ ( $0.1 \mu_B/V$ )	$R(Q)$ ( $0.082 \mu_B/\text{basal V}$ ; $0.155 \mu_B/\text{apical V}$ )	$R(Q)$ ( $0.4 \mu_B/\text{apical V}$ )
1, 1, 1	d1 (1, 1, 1)	0.76	0.84	1.29
	d2 (0, 0, -1), d3 (0, -1, 0), d4 (-1, 0, 0)	0.76	0.74	0.65
0, 0, 2	d1 (1, 1, 0), d2 (1, 1, 0), d3 (-1, -1, 0), d4 (-1, -1, 0)	1.25	1.24	1.18
2, 2, 0	d1 (1, 1, 2), d2 (-1, -1, -2)	1.03	0.93	0.60
	d3 (1, -1, 0), d4 (-1, 1, 0)	1.04	1.15	1.80
1, 1, 3	d1 (2, 2, 1)	1.11	1.21	1.76
	d3 (-1, -2, 0), d4 (-2, -1, 0)	1.15	1.16	1.24
	d2 (1, 1, -1)	1.13	1.03	0.66
2, 2, 2	d1 (2, 2, 2)	0.85	0.85	0.85
	d2 (0, 0, -2), d3 (0, -2, 0), d4 (-2, 0, 0)	0.86	0.86	0.86
0, 0, 4	d1 (2, 2, 0), d2 (2, 2, 0), d3 (-2, -2, 0), d4 (-2, -2, 0)	1.32	1.32	1.33
3, 3, 1	d1 (2, 2, 3)	0.87	0.87	0.87
	d2 (-1, -1, -3)	0.89	1.00	1.70
	d3 (1, -2, 0), d4 (-2, 1, 0)	0.89	0.84	0.64
2, 2, 4	d1 (3, 3, 2)	1.11	1.19	1.63
	d3 (-1, -3, 0), d4 (-3, -1, 0)	1.08	1.00	0.71
	d2 (1, 1, -2)	1.08	1.17	1.65
3, 3, 3	d1 (3, 3, 3)	0.85	0.78	0.52
	d2 (0, 0, -3), d3 (0, -3, 0), d4 (-3, 0, 0)	0.83	0.86	1.03
4, 4, 0	d1 (2, 2, 4), d2 (-2, -2, -4)	1.13	1.13	1.11
	d3 (2, -2, 0), d4 (-2, 2, 0)	1.12	1.13	1.17

have the same  $Q$  value. When taking a cut along the  $(H, H, H)$  direction, as we would when collecting flipping ratio data, the multiple peaks are clearly seen, as shown in the top panel of Fig. S3(b). The sample quality, however, is not to blame, as the multiple crystallites form a single crystallite when the temperature is raised above that of the Jahn-Teller distortion, as seen in the bottom panel of Fig. S3(b) at  $T = 50$  K. This reversible process was seen at other Bragg peak positions. We were not able to reliably assign which domain contributed to which peak for all peaks seen. The course resolution used for the  $T = 15$  K and  $T = 20$  K data integrated over all domains and crystallites, avoiding this problem. Course resolution data were taken for  $T = 3$  K, but the analysis was inconclusive, which is why we initially attempted the high resolution measurements. It was then that we found

the moments could not be fully field polarized with 2 T at  $T = 3$  K.

### ANALYSIS OF DENSITY FUNCTIONAL THEORY RESULTS

To understand the low-temperature ferromagnetism in  $\text{GaV}_4\text{S}_8$  and its behavior in the presence of electron correlations, density functional theory (DFT) calculations were carried out with the inclusion of on-site Coulomb repulsion incorporated via a simplified rotationally-invariant DFT+ $U_{\text{eff}}$  method [3]. For the test of how  $\text{GaV}_4\text{S}_8$  behaves under different choices of exchange-correlation functionals, we employed the Ceperley-Alder parametrization of the local-density ap-

proximation (LDA), [4] the Perdew-Burke-Ernzerhof generalized-gradient approximation (PBE), [5] and the variant of PBE for crystalline solids (PBEsol). [6] For the choice of DFT code and computational parameters, refer to the Methods section in the main text. The unit cell volume at ambient conditions was optimized for each choice of exchange-correlation functional and  $U_{\text{eff}}$  value, after which the rhombohedral angle  $\alpha$  was varied at fixed volume. A collinear ferromagnetic initial condition was chosen for all calculations, and it was checked that an intra- $V_4$ -cluster antiparallel arrangement of  $V$  spin moments could only be stabilized in the H-FM (high-spin configuration) phases.

Fig. S4 and Table SIV summarize the DFT+ $U_{\text{eff}}$  results, showing the behavior of the total energy and magnetism as a function of  $\alpha$ . Therein NM, L-FM, and H-FM stand for nonmagnetic,  $S = 1/2$  low-spin, and  $S = 5/2$  (LDA) or  $7/2$  (PBE/PBEsol) high-spin configurations as discussed in Ref. 7. Several features of computational results are noteworthy:

- The magnetism and rhombohedral distortion are strongly coupled to each other. In particular, the experimentally found rhombohedral distortion of  $\alpha \approx 59.6^\circ$  [8] is only reproduced in the L-FM configuration with small  $U_{\text{eff}}$  of  $\leq 2$  eV. This is because (i) the bulk dipole moment cannot be stabilized in the metallic NM phase and (ii) the H-FM phases do not have strong Jahn-Teller instabilities like the L-FM case, due to the closed-shell orbital configuration and weaker  $V_4$  clustering. [7]
- Employing no  $U_{\text{eff}}$ , except for the LDA case, results in a strongly localized spin moment distribution at the apical  $V$  site (denoted as Phase 2 hereafter

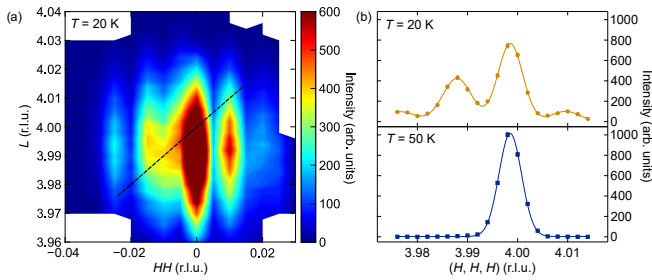


FIG. S3. (a) Map of the  $(H, H, L)$  plane about the cubic  $(0, 0, 4)$  peak at  $T = 20$  K taken with the high instrumental resolution. Splitting of the peak is along the mosaic direction, such that all peaks have the same  $Q$ . The dashed line shows a cut along the  $(H, H, H)$  direction, and this cut is shown in panel (b) at two different temperatures. The top shows the same temperature,  $T = 20$  K, as in (a). This is below the Jahn-Teller transition temperature where four crystallographic domains are expected. The bottom panel shows the same  $(H, H, H)$  cut at  $T = 50$  K. The single peak shows that the crystallite formation beneath the Jahn-Teller distortion is reversible.

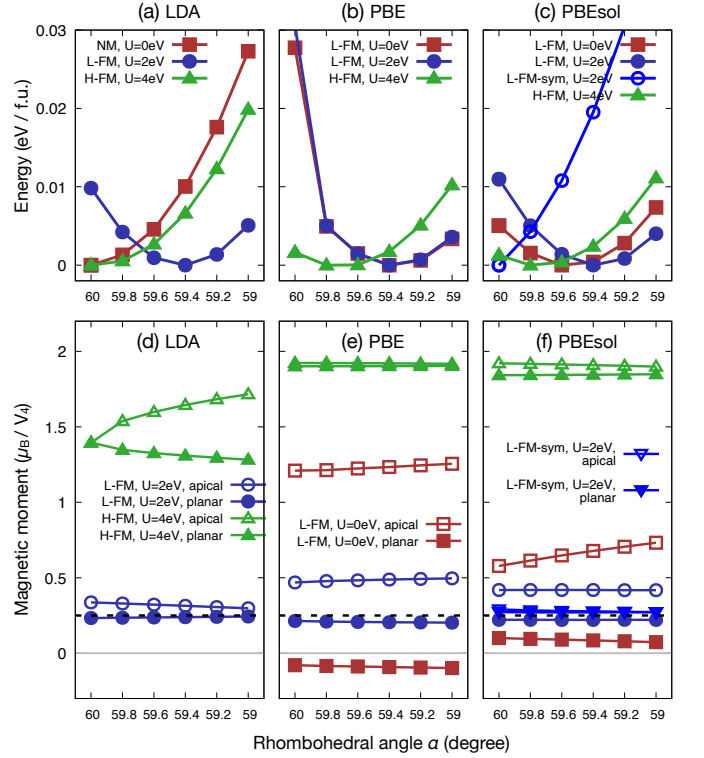


FIG. S4. Plots of (a-c) total energy and (d-f) magnetic moment values as a function of rhombohedral angle  $\alpha$  at different  $U_{\text{eff}}$ , where spin moments of apical and planar  $V$  sites are separately shown in (d-f). NM, L-FM, and H-FM stand for nonmagnetic, low-spin ferromagnetic, and high-spin ferromagnetic phases, respectively.

and in Table SIV), which remains stable as  $U_{\text{eff}}$  is included. This localization of the spin moment seems to emerge from the momentum space dispersion of the partially filled  $T^2$  molecular orbital triplet band. Interestingly, introducing  $U_{\text{eff}}$  facilitates the convergence of phases with more equally distributed spin density over the 4  $V$  sites in the  $V_4$  cluster (denoted as Phase 1), while phase 2 is lower in energy over the whole  $U_{\text{eff}}$ -range in the PBEsol case (see Table SIV). The spin localization is strongest in the PBE functional results, and weakest in the LDA case.

- Table SIV summarizes the computed structural parameters and  $V$ -site magnetizations obtained from two different local minima states (Phase 1 and 2). [9] Note that the presence of more than one local minima state in  $\text{GaV}_4\text{S}_8$  is also noticed in a recent DFT+ $U$  computational study. [10] Phase 1 in Table SIV shows spin moments which are close to equi-distributed over all  $V$  sites, while the spin moments starting from phase 2 are mostly localized at the apical  $V$  site. Phase 2 corresponds to the data presented in Ref. 10 and, as mentioned

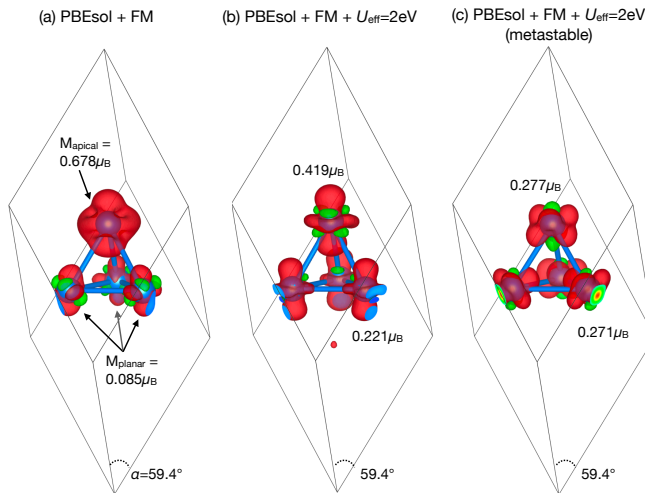


FIG. S5. Spin density isosurfaces of  $\text{GaV}_4\text{S}_8$  from PBEsol+ $U_{\text{eff}}$  density functional calculations with different  $U_{\text{eff}}$  values: (a) at  $U_{\text{eff}} = 0$  eV and (b,c)  $U_{\text{eff}} = 2$  eV, where (b) and (c) are from the ground and metastable configurations respectively. Spin densities are plotted by employing a rhombohedral angle  $\alpha = 59.4^\circ$ , and black lines depict the primitive unit cell.

therein, is lower in energy than phase 1 by 0.1 ~ 0.3 eV per formula unit depending on the value of  $U_{\text{eff}}$ . Phase 1, on the other hand, is more consistent with the measured spin distribution in this work, and it also captures better agreements of the rhombohedral angle  $\alpha$  and the degree of  $\text{V}_4$  elongation ( $dV-V_{\text{ap}} / dV-V_{\text{pl}}$ ) between theory and experiments around  $U_{\text{eff}} = 1$  eV. Hence we focus on the phase 1 results in this study because of its better agreement of physically important parameters (spin distribution, rhombohedral angle, and the degree of  $\text{V}_4$  cluster elongation) with experiments.

- The results of the calculations are strongly dependent on the initial conditions, suggesting multiple local-minima states in this system. Specifically in the PBEsol functional results, three configurations with different spin moment distributions can be obtained around  $U_{\text{eff}} = 2$  eV; even within phase 1, two different patterns of the spin distribution occur (Figs. 4(c) and (f), and Figs. 5(b) and (c)). The case with equally distributed spin moments, while higher in energy, favors a cubic structure, while the ground state configuration with an imbalanced spin moment distribution favors a rhombohedrally distorted phase. Their total energies versus the rhombohedral angle are shown in Figs. 4(c) and (f).

The presence of multiple local minima states in the low-temperature phase of  $\text{GaV}_4\text{S}_8$  implies a complicated interplay between the charge, orbital, spin, and lattice degrees of freedom in this system. Further, it was suggested recently that inter-site correlation effects may also be crucial in understanding several structural properties of this compound even in the high-temperature cubic phase. [7] Hence more elaborate computational studies of  $\text{GaV}_4\text{S}_8$  beyond the DFT+ $U$  level should follow for a better understanding of the ground state and multiferroic properties.

- 
- [1] I. Kézsmárki, S. Bordács, P. Milde, E. Neuber, L. M. Eng, J. S. White, H. M. Rønnow, C. D. Dewhurst, M. Mochizuki, K. Yanai, H. Nakamura, D. Ehlers, V. Tsurkan, and A. Loidl, Neel-type skyrmion lattice with confined orientation in the polar magnetic semiconductor  $\text{GaV}_4\text{S}_8$ , *Nat. Mater.* **14**, 1116 (2015).
  - [2] W. Williams, *Polarized Neutrons*, Oxford science publications (Clarendon Press, 1988).
  - [3] S. L. Dudarev, G. A. Botton, S. Y. Savrasov, C. J. Humphreys, and A. P. Sutton, Electron-energy-loss spectra and the structural stability of nickel oxide: An LSDA+ $U$  study, *Phys. Rev. B* **57**, 1505 (1998).
  - [4] D. M. Ceperley and B. J. Alder, Ground State of the Electron Gas by a Stochastic Method, *Phys. Rev. Lett.* **45**, 566 (1980).
  - [5] J. P. Perdew, K. Burke, and M. Ernzerhof, Generalized Gradient Approximation Made Simple, *Phys. Rev. Lett.* **77**, 3865 (1996).
  - [6] G. I. Csonka, J. P. Perdew, A. Ruzsinszky, P. H. T. Philipsen, S. Lebègue, J. Paier, O. A. Vydrov, and J. G. Ángyán, Assessing the performance of recent density functionals for bulk solids, *Phys. Rev. B* **79**, 155107 (2009).
  - [7] H.-S. Kim, K. Haule, and D. Vanderbilt, Molecular Mott States in Deficient Spinel  $\text{GaV}_4\text{S}_8$ , arXiv:1810.09495 (2018).
  - [8] R. Pocha, D. Johrendt, and R. Pöttgen, Electronic and Structural Instabilities in  $\text{GaV}_4\text{S}_8$  and  $\text{GaMo}_4\text{S}_8$ , *Chem. Mater.* **12**, 2882 (2000).
  - [9] Note that an enhanced plane-wave energy cutoff of 500 eV was employed to generate data shown in this table for more accurate total energy comparison, which yields slightly different sizes of vanadium spin moments compared to shown in Fig. S5.
  - [10] Y. Wang, D. Puggioni, and J. M. Rondinelli, Assessing exchange-correlation functional performance in the chalcogenide lacunar spinels  $\text{GaM}_4\text{Q}_8$  ( $M = \text{Mo, V, Nb, Ta}$ ;  $Q = \text{S, Se}$ ), *Phys. Rev. B* **100**, 115149 (2019).
  - [11] A. V. Powell, A. McDowall, I. Szkoda, K. S. Knight, B. J. Kennedy, and T. Vogt, Cation Substitution in Defect Thiospinels: Structural and Magnetic Properties of  $\text{GaV}_{4-x}\text{Mo}_x\text{S}_8$  ( $0 \leq x \leq 4$ ), *Chemistry of Materials*, *Chemistry of Materials* **19**, 5035 (2007).

TABLE SIV. Summary of PBEsol+ $U_{\text{eff}}$  calculation results in the low-temperature rhombohedral phase, in comparison with experimentally measured structural parameters from Ref. 8 and 11. Below  $dV - V_{\text{ap}}$  and  $dV - V_{\text{pl}}$  are the longer and shorter intra-cluster V-V distances, respectively.  $M - V_{\text{ap}}$  and  $M - V_{\text{pl}}$  denote magnetization at the apical and planar V-sites in the  $V_4$  cluster. Total energies per formula unit of phase 1 and 2 from VASP calculations,  $E_1$  and  $E_2$  respectively, and their difference at the same  $U_{\text{eff}}$  value are shown also.

Phase 1										
$U_{\text{eff}}$ (eV)	$a$ (Å)	$\alpha$ (deg.)	$dV - V_{\text{ap}}$ (Å)	$dV - V_{\text{pl}}$ (Å)	$\frac{dV - V_{\text{ap}}}{dV - V_{\text{pl}}}$	$M - V_{\text{ap}}$ ( $\mu_{\text{B}}$ )	$M - V_{\text{pl}}$ ( $\mu_{\text{B}}$ )	Gap size (eV)	$E$ (eV/f.u.)	$E_1 - E_2$ (eV/f.u.)
1.0	6.780	59.500	2.865	2.746	1.043	0.249	0.252	0.270	-85.408	0.116
1.5	6.792	59.431	2.881	2.743	1.050	0.361	0.231	0.375	-83.342	0.224
2.0	6.804	59.383	2.899	2.742	1.057	0.426	0.220	0.569	-81.297	0.356
Phase 2										
0	6.765	59.534	2.853	2.749	1.038	0.686	0.082	0.000	-89.615	
0.5	6.791	59.354	2.893	2.752	1.051	1.200	-0.083	0.110	-87.538	
1.0	6.813	59.263	2.925	2.763	1.059	1.505	-0.189	0.167	-85.524	
1.5	6.832	59.199	2.951	2.776	1.063	1.710	-0.271	0.239	-83.566	
2.0	6.851	59.140	2.975	2.789	1.067	1.875	-0.346	0.309	-81.653	
Exp. results										
Pocha et al. LT, 20K	6.834	59.660	2.898	2.826	1.025					
Powell et al. LT, 20K	6.839	59.643	2.943	2.856	1.030					
Powell et al. LT, 4.2K	6.840	59.616	2.920	2.846	1.026					